

Broad emission band of Yb³⁺ in the nonlinear Nb:RbTiOPO₄ crystal: origin and applications

J. J. Carvajal,^{1,*} G. Ciatto,² X. Mateos,^{1,3} A. Schmidt,³ U. Griebner,³ V. Petrov,³ G. Boulon,⁴ A. Brenier,⁴ A. Peña,^{1,5} M. C. Pujol,¹ M. Aguiló,¹ and F. Díaz¹

¹Física i Cristal·lografia de Materials i Nanomaterials (FiCMA-FiCNA), Universitat Rovira i Virgili (URV), Campus Sescelades c/Marcel·lí Domingo s/n, E-43007 Tarragona, Spain

²Synchrotron SOLEIL, L'Orme des Merisiers, Saint-Aubin, BP 48, 91192 Gif sur Yvette Cedex, France

³Max Born Institute for Nonlinear Optics and Ultrafast Spectroscopy, 2A Max-Born-Str., D-12489 Berlin, Germany

⁴Laboratoire de Physico-Chimie de Matériaux Luminescents, Université Claude Bernard, 69622 Villeurbanne, France

⁵Institut Néel/CNRS-UJF, 25 avenue des Martyrs-BP 166, F-38402 Grenoble, France

*joan josep.carvajal@urv.cat

Abstract: By means of micro-structural and optical characterization of the Yb:Nb:RbTiOPO₄ crystal, we demonstrated that the broad emission band of Yb³⁺ in these crystals is due to the large splitting of the ytterbium ground state only, and not to a complex multisite occupation by the ytterbium ions in the crystals. We used this broad emission band to demonstrate wide laser tuning range and generation of femtosecond laser pulses. Passive mode-locked laser operation has been realized by using a semiconductor saturable absorber mirror, generating ultra short laser pulses of 155 fs, which were very stable in time, under Ti:sapphire laser pumping at 1053 nm.

©2010 Optical Society of America

OCIS codes: (140.7090) Ultrafast lasers; (160.4330) Nonlinear optical materials.

References and links

1. A. Ishibashi, "II-VI blue-green light emitters," *J. Cryst. Growth* **159**(1-4), 555–565 (1996).
2. S. Nakamura, M. Senoh, S. Nagahama, N. Iwasa, T. Yamada, T. Matsushita, H. Kiyoku, and Y. Sugimoto, "InGaN-based multi-quantum-well-structure laser diodes," *Jpn. J. Appl. Phys.* **35**(Part 2, No. 1B), L74–L76 (1996).
3. D. F. Eaton, "Nonlinear optical materials," *Science* **253**(5017), 281–287 (1991).
4. R. H. Stolen, and H. W. K. Tom, "Self-organized phase-matched harmonic generation in optical fibers," *Opt. Lett.* **12**(8), 585–587 (1987).
5. K. Mizuuchi, K. Yamamoto, and T. Taniuchi, "Second-harmonic generation of blue light in a LiTaO₃ waveguide," *Appl. Phys. Lett.* **58**(24), 2732–2734 (1991).
6. X. Mateos, F. Güell, M. C. Pujol, M. A. Bursukova, and R. Solé, "Green luminescence of Er³⁺ in stoichiometric KYb(WO₄)₂ single crystals," *Appl. Phys. Lett.* **80**, 4510–4512 (2002).
7. M. Oomen, "Upconversion in fluoride glass fibers," *Adv. Mater.* **3**(7-8), 403–406 (1991).
8. A. Brenier, "The self-doubling and summing lasers: overview and modeling," *J. Lumin.* **91**(3-4), 121–132 (2000).
9. R. Solé, V. Nikolov, I. Koseva, P. Peshev, X. Ruiz, C. Zaldo, M. J. Martín, M. Aguiló, and F. Díaz, "Conditions and possibilities for rare-earth doping of KTiOPO₄ flux-grown single crystals," *Chem. Mater.* **9**(12), 2745–2749 (1997).
10. C. Zaldo, M. Rico, J. J. Carvajal, and F. Díaz, "Progress in crystal growth and characterisation of rare-earth doped non-linear KTP crystals for laser applications," *Opt. Mater.* **13**(1), 175–180 (1999).
11. J. J. Carvajal, V. Nikolov, R. Solé, J. Gavaldà, J. Massons, M. Rico, C. Zaldo, M. Aguiló, and F. Díaz, "Enhancement of the erbium concentration in RbTiOPO₄ by codoping with niobium," *Chem. Mater.* **12**(10), 3171–3180 (2000).
12. J. J. Carvajal, V. Nikolov, R. Solé, J. Gavaldà, J. Massons, M. Aguiló, and F. Díaz, "Crystallization region, crystal growth, and characterization of rubidium titanyl phosphate codoped with niobium and lanthanide ions," *Chem. Mater.* **14**(7), 3136–3142 (2002).
13. A. Peña, J. J. Carvajal, M. C. Pujol, X. Mateos, M. Aguiló, F. Díaz, V. Petrov, P. Segonds, and B. Boulanger, "Yb(³⁺) spectroscopy in (Nb or Ta):RbTiOPO₄ single crystals for laser applications," *Opt. Express* **15**(22), 14580–14590 (2007).
14. L. K. Cheng, J. D. Bierlein, and A. A. Ballman, "Crystal growth of KTiOPO₄ isomorphs from tungstate and molybdate fluxes," *J. Cryst. Growth* **110**(4), 697–703 (1991).
15. J. J. Carvajal, R. Solé, J. Gavaldà, J. Massons, M. Aguiló, and F. Díaz, "Crystal growth of RbTiOPO₄:Nb: a new nonlinear optical host for rare earth doping," *Cryst. Growth Des.* **1**(6), 479–484 (2001).

16. J. J. Carvajal, C. F. Woensdregt, R. Solé, F. Díaz, and M. Aguiló, "Change in morphology of RbTiOPO₄ introduced by the presence of Nb," *Cryst. Growth Des.* **6**(12), 2667–2673 (2006).
17. J. L. Pouchou, and F. Pichoir, "New model quantitative x-ray microanalysis, I. Application to the analysis of homogenous samples," *Rech. Aerosp.* **3**, 13–38 (1984).
18. X. Mateos, V. Petrov, A. Peña, J. J. Carvajal, M. Aguiló, F. Díaz, P. Segonds, and B. Boulanger, "Laser operation of Yb³⁺ in the acentric RbTiOPO₄ codoped with Nb⁵⁺," *Opt. Lett.* **32**(13), 1929–1931 (2007).
19. A. Filipponi, M. Borowski, D. T. Bowron, S. Ansell, A. D. Cicco, S. D. Panfilis, and J. P. Itié, "An experimental station for advanced research on condensed matter under extreme conditions at the European Synchrotron Radiation Facility-BM29 beamline," *Rev. Sci. Instrum.* **71**(6), 2422–2432 (2000).
20. J. Jaklevic, J. A. Kirby, M. P. Klein, A. S. Robertson, G. S. Brown, and P. Eisenberger, "Fluorescence detection of exafs: sensitivity enhancement for dilute species and thin films," *Solid State Commun.* **23**(9), 679–682 (1977).
21. J. J. Carvajal, J. L. García-Muñoz, R. Solé, J. Gavalda, Massons, X. Solans, F. Díaz, and M. Aguiló, "Charge self-compensation in the non-linear optical crystals Rb_{0.855}Ti_{0.955}Nb_{0.045}OPO₄ and RbTi_{0.927}Nb_{0.056}Er_{0.017}OPO₄," *Chem. Mater.* **15**(12), 2338–2345 (2003).
22. A. L. Ankudinov, B. Ravel, J. J. Rehr, and S. D. Conradson, "Real-space multiple-scattering calculation and interpretation of x-ray absorption near-edge structure," *Phys. Rev. B* **58**(12), 7565–7576 (1998).
23. B. Ravel, and M. Newville, "ATHENA, ARTEMIS, HEPHAESTUS: data analysis for X-ray absorption spectroscopy using IFEFFIT," *J. Synchrotron Radiat.* **12**(4), 537–541 (2005).
24. P. A. Thomas, S. C. Mayo, and B. E. Watts, "Crystal structures of RbTiOAsO₄, KTiO(P_{0.58}, As_{0.42})O₄, RbTiOPO₄ and (Rb_{0.465}, K_{0.535})TiOPO₄, and analysis of pseudosymmetry in crystals of the KTiOPO₄ family," *Acta Crystallogr. B* **48**(4), 401–407 (1992).
25. J. J. Carvajal, and R. Solé, "A new self-doubling material: RbTiOPO₄:(Nb,Ln)," *Opt. Mater.* **24**(1-2), 425–430 (2003).
26. M. Vaccari, and P. Fornasini, "Einstein and Debye models for EXAFS parallel and perpendicular mean-square relative displacements," *J. Synchrotron Radiat.* **13**(4), 321–325 (2006).
27. J. J. Carvajal, G. Ciatto, A. Peña, M. C. Pujol, J. Gavalda, F. Díaz, and M. Aguiló, "Lattice location and short range ordering of doping ions in RbTiOPO₄," *Appl. Phys. Lett.* **94**(6), 061908 (2009).
28. J. J. Carvajal, J. L. García-Muñoz, and R. Solé, "Selective distribution of dopants among MO₆ octahedra in RbTi_{0.927}Nb_{0.056}Er_{0.017}OPO₄: a neutron diffraction study," *J. Solid State Chem.* **171**(1-2), 257–261 (2003).
29. R. Ternane, G. Boulon, Y. Guyot, M. T. Cohen-Adad, M. Trabelsi-Ayedi, and N. Kbir-Arigoib, "Crystal growth, structural and spectroscopic characterization of undoped and Yb³⁺-doped oxyboropate fibers," *Opt. Mater.* **22**(2), 117–128 (2003).
30. G. Boulon, A. Collombet, A. Brenier, M. T. Cohen-Adad, A. Yoshikawa, K. Lebbou, J. Lee, and T. Fukuda, "Structural and spectroscopic characterization of nominal Yb³⁺:Ca₈La₂(PO₄)₆O₂ oxyapatite subgle crystal fibers grown by the micro-pulling-down method," *Adv. Funct. Mater.* **11**(4), 263–270 (2001).
31. G. Boulon, A. Brenier, L. Laversenne, Y. Guyot, C. Goutaudier, M. T. Cohen-Adad, G. Métrat, and N. Muhlstein, "Search of optimized trivalent ytterbium doped-inorganic crystals for laser applications," *J. Alloy. Comp.* **341**(1-2), 2–7 (2002).
32. V. V. Ovsyankin, *Spectroscopy of Solids Containing Rare Earth Ions* (Elsevier Science, 1987).
33. J. J. Carvajal, and R. Solé, "Spectroscopic and second harmonic generation properties of a new crystal: Yb-doped RbTiOPO₄," *Opt. Mater.* **26**(3), 313–317 (2004).
34. A. Peña, J. J. Carvajal, J. Massons, J. Gavalda, F. Díaz, and M. Aguiló, "Yb:Ta:RbTiOPO₄, a new strategy to further increase the lanthanide concentration in crystals of the KTiOPO₄ family," *Chem. Mater.* **19**(16), 4069–4076 (2007).

1. Introduction

In the last years, an increasing interest in the development of compact blue and green laser sources for applications such as high-density optical data storage, color projection, laser printing, and medical applications is evident [1]. This intensification of the research in these fields has been boosted by recent and promising achievements in the field of wide band-gap semiconductor diode lasers [2], harmonic generation in nonlinear optical (NLO) bulk crystals [3], optical fibers [4] and other waveguides [5], and up conversion lasers in crystals [6] and fibers [7].

A class of such sources comprises NLO crystals with suitable sites for active lanthanide ions, such as Yb³⁺ and Nd³⁺ ions, in which the 1 μm emission of these ions is combined with the second harmonic generation properties of the host to produce green-laser radiation by self-frequency doubling [8], supplying a strategy to reduce the complexity and size of the devices based on these materials. So, there exists interest on finding non-centrosymmetric crystal hosts which allow doping levels high enough to obtain laser operation.

KTiOPO₄ (KTP) is a non-centrosymmetric crystal that crystallizes in the orthorhombic system with space group of symmetry Pna2₁, and exhibits large nonlinearities and a high damage threshold. However, doping this crystal with lanthanide active ions is rather difficult because the crystal structure does not contain an equivalent passive ion belonging to the same

series of elements [9]. RbTiOPO₄ (RTP), which belongs to the same family of materials as KTP and shows similar nonlinear properties, was successfully doped with lanthanide ions such as erbium and ytterbium [10]. The larger structure of RTP when compared to that of KTP due to the large ionic radius of Rb⁺ allowed this doping. The doping level of lanthanide ions in RTP increased by codoping with niobium, on the basis of charge compensation [11], resulting in ytterbium concentrations as high as $\sim 2 \times 10^{20}$ at·cm⁻³ [12].

Solid state lasers based on ytterbium have been studied intensively as an alternative to neodymium-based solid state lasers for ~ 1 μ m operation. Ytterbium has a simple energy level scheme when compared to neodymium, which helps to avoid various loss mechanisms. Furthermore, the smaller quantum defect that this ion presents due to the proximity between the absorbing and emitting levels leads to reduced heat generation. Finally, its broad fluorescence band, due to the electron-phonon coupling, makes ytterbium doped materials interesting for tunable or femtosecond laser operation.

In this work we report what is, to the best of our knowledge, the first mode-locked ytterbium laser employing a member of the KTP family of nonlinear crystals, Yb:Nb:RTP. We also identify the origin of the extremely broad emission band observed in these crystals [13]. A detailed knowledge of the local environment around the doping ions, in particular of their precise location inside the RTP lattice, of their atomic neighborhood, and of the bond lengths distribution and distortions is very important because the presence of lanthanide ions in one or more crystallographic sites with defined symmetry determines the features of the optical absorption spectra of these materials. Indeed, the use of a local structural tool, such as Extended X-ray Absorption Fine structure Spectroscopy (EXAFS), was necessary for understanding the origin of the material optical spectroscopic properties. By combining this technique with the optical spectroscopic characterization of Yb:Nb:RTP crystals we have been able to determine that their broad emission band is due only to the large Stark splitting of the electronic states of Yb³⁺ ions in this matrix and not to a multisite location of Yb³⁺ in these crystals.

2. Crystal growth, X-ray diffraction, and concentration analysis

RTP and isostructural crystals cannot be grown directly by conventional techniques from the melt since these crystals melt incongruently [14]. Yb:Nb:RTP single crystals have been grown by high temperature solution based methods, and in particular by the top-seeded solution growth (TSSG) technique with slow cooling (SC) of the solution [12].

So, we grew Yb:Nb:RTP single crystals in self-fluxes with a composition of Rb₂O-P₂O₅-TiO₂-Nb₂O₅-Yb₂O₃ = 40.8-27.2-30.4-0.96-0.64 mol % to avoid the presence of alien ions that can alter the physical properties of the crystals. This solution composition was chosen because it is in the middle of the crystallization region of RTP [11], and we can avoid the crystallization of other undesired phases. Furthermore, this solution composition corresponds to the one that allowed us to obtain a higher concentration of Yb³⁺ in the crystals [12]. The solution, with a weight of around 120 g, was prepared by mixing the appropriate amounts of the initial reagents, Rb₂CO₃, NH₄H₂PO₄, TiO₂, Nb₂O₅, and Yb₂O₃, all with a 99% purity or higher, in a 125 cm³ cylindrical platinum crucible, 6.5 cm in height and 5.0 cm in diameter. All the growth experiments were performed in a vertical tubular single-zone furnace with a Kanthal AF resistance heating wire [15], with a useful thermal zone of 30 cm in length and 7.5 cm in diameter. The temperature of the furnace was controlled by a Eurotherm 903 controller/programmer connected to a thyristor. The solution was homogenized by maintaining it at a temperature of about 50-100 K above the expected saturation temperature for 3-5 h. The axial temperature gradient in the solution was 1.3 K cm⁻¹ along the first 1 cm and 0.8 K cm⁻¹ along the next 1.5 cm, with the bottom of the crucible being always hotter than the surface of the solution. The radial gradient was constant and amounted to 1.8 K cm⁻¹.

We used *c*-oriented Yb:Nb:RTP prismatic crystal seeds with the same chemical composition of the crystal to be grown for the single crystal growth experiments. The crystal seeds had dimensions of 5.0 × 1.5 × 5.0 mm in the *a* × *b* × *c* crystallographic directions. In

this way we forced the growth of the crystal along the a crystallographic axis, obtaining more isometric single crystals, and avoiding the flat morphology induced by the presence of Nb in the crystals [16]. We fixed the crystal seed to a growth device that included a platinum turbine immersed in the solution. The crystal seed was off-set some millimeters from the rotation axis of the turbine [11]. In all experiments the crystal seed and the platinum turbine were rotated together at a constant angular speed of 65 rpm and the direction of rotation was changed every 50 s.

We determined the saturation temperature (T_s) by inspecting the growth or dissolution of the crystal seed in contact with the surface of the solution. The typical growth process was carried out by decreasing the temperature by 17 K at a variable cooling rate: first by 1 K at 1 K/h, then by 6 K at 0.05 K/h, and finally by 10 K at a cooling rate of 0.03 K/h. Larger cooling intervals or faster cooling rates resulted in spurious nucleation on the surface of the solution or on the platinum turbine. When the cooling program was completed, the grown crystal and the platinum turbine were lifted slowly until the bottom of the Pt turbine was located 5-10 mm above the surface of the solution. Then, the furnace was cooled down to room temperature at a rate of 15 K h⁻¹, while keeping the crystal inside the furnace to avoid thermal stress that could result in cracks in the crystal. The experiments lasted 4 weeks on average.

Defect free Yb:Nb:RTP bulk single crystals with maximum dimensions of 6 × 16 × 12 mm along the a , b and c crystallographic directions, and weights around 2.5 g were obtained by the TSSG-SC method from a self-flux solution. Figures 1(a) and 1(b) show one of the Yb:Nb:RTP crystals obtained in these crystal growth experiments.

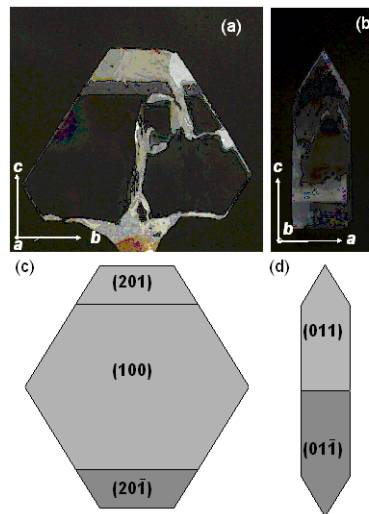


Fig. 1. Pictures of a Yb:Nb:RTP single crystal obtained by the TSSG-SC method in views (a) perpendicular to the a crystallographic axis, and (b) perpendicular to the b axis. (c) and (d) Schematic representation of its morphology along the same directions.

X-ray powder diffraction was used to assess that the crystals grown were isostructural to RTP, although the morphology of the crystals already constituted a proof of their isostructurality. The characterization was performed in a Bruker-AXS D8-Discover diffractometer with parallel incident beam (Göbel mirror) and vertical θ - θ goniometer, a 0.02° receiving slit and a scintillation counter as a detector. The angular 2θ diffraction range was set between 5° and 70°. The data were collected with an angular step of 0.02° at 16 s per step. Cu radiation was obtained from a copper X-ray tube operated at 40 kV and 40 mA. For this characterization we used a piece of the as grown crystal that was ground to a homogeneous grain size of 5-20 μm using an agate mortar. The crystals were cleaned with distilled water to eliminate any rests of solution.

Figure 2 shows the X-ray powder diffraction pattern corresponding to these Yb:Nb:RTP and RTP. The X-ray diffraction pattern of pure RTP is included for comparison together with the standard of RTP included in the JCPDS-ICDD database (01-81-0552). As expected, the Yb:Nb:RTP crystals are isostructural to RTP, crystallizing in the orthorhombic system, with the $Pna2_1$ space group. No other phases were observed by X-ray powder diffraction.

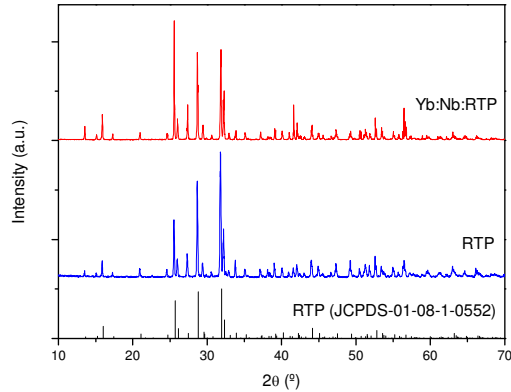


Fig. 2. X-ray powder diffraction pattern of Yb:Nb:RTP and RTP, and the standard of RTP included in the JCPDS-ICDD.

The morphology of the crystal is formed by the $\{100\}$, $\{201\}$, $\{20\bar{1}\}$, $\{011\}$, and $\{01\bar{1}\}$ forms. Figures 1(c) and 1(d) also shows schematic representations of the calculated morphology for these crystals. When we compared the morphology of the crystals obtained with the morphology of pure RTP crystals [11], we observed that the $\{110\}$ form of the crystals disappeared completely, while the $\{011\}$ and the $\{01\bar{1}\}$ forms show a great presence in these new crystals. This is similar to the morphology observed previously for Nb:RTP crystals grown with the same methodology, although in that case the $\{110\}$ form could still be seen despite its low area [16]. This modified morphology forced by the use of thick crystal seeds along the a crystallographic direction provides a larger useful crystal area in the x - y plane when compared to the morphology of crystals grown using thin crystal seeds along the a crystallographic direction. This is the plane where the phase-matching direction of this family of materials is located, and so, it has benefits for further applications in second-harmonic generation and self-frequency doubling.

Yb and Nb in the as grown crystals were analyzed by electron probe microanalysis (EPMA) in a Cameca SX50 microprobe analyzer operating in the wavelength-dispersive mode. The concentration of Nb was analyzed at 30 nA electron current and the concentration of Yb at 100 nA. The accelerating voltage was kept at 25 kV in all cases. LiNbO_3 and YbF_3 were used as standards for Nb and Yb. The analyses were performed using the Nb $L\alpha$ line measured with a PET crystal, and the Yb $L\alpha$ line measured with a LiF crystal. The measurements were integrated during 10 s. The raw intensities were corrected for dead time, background, and matrix effects using the PAP correction procedure [17].

The Yb^{3+} concentration achieved in these crystals, measured by the EPMA technique, was 2×10^{20} $\text{at}\cdot\text{cm}^{-3}$ (2.2 at. %), which resulted in a stoichiometry for the crystal of $\text{RbTi}_{0.95}\text{Yb}_{0.02}\text{Nb}_{0.03}\text{OPO}_4$. This concentration has been shown to be high enough to obtain laser action from Yb^{3+} in these crystals [18], and it is more than 3 times larger than that obtained for RTP crystals doped only with Yb^{3+} ($\sim 6 \times 10^{19}$ $\text{at}\cdot\text{cm}^{-3}$).

3. EXAFS characterization

We analyzed the local environment of Yb^{3+} in Yb:Nb:RTP crystals by EXAFS at the Yb L3-edge. The experiment was performed at the BM29 beam line [19] of the European

Synchrotron Radiation Facility (ESRF) by using a Si (111) double crystal monochromator; high order-harmonics were rejected by using Si mirrors and detuning the monochromator crystals. Detection was performed in fluorescence mode by using a thirteen element Ge hyperpure detector. The high dilution of Yb atoms in the crystals ensured the linear proportionality between the fluorescence intensity and the absorption cross section [20]. Samples were measured at room temperature at an incidence angle of 45° for the X-ray beam.

The X-ray absorption spectra were pre-edge and background subtracted (using a linear function and cubic spline, respectively), and normalized to the jump to obtain $\chi(k)$ spectra. Then, the k -range [$3.0 - 11.8 \text{ \AA}^{-1}$] of the $\chi(k)$ EXAFS spectra was selected, weighted by k^1 , and multiplied by a Hanning window ($dk = 3$) before being Fourier-transformed, together with theoretical signals, to the real space for quantitative analysis. The R -range [$1.1 - 4.4 \text{ \AA}$] was selected to perform fits. The theoretical signals employed in the fits were calculated using clusters in which the positions of Rb, Ti, O, P and Nb atoms were taken from previous neutron diffraction analysis [21], and substituting a Yb atom in the different possible sites of interest (Ti-1, Ti-2, Rb-1, Rb-2) without relaxation of the interatomic distances (we allow relaxation during the fitting step).

The FEFF 8.0 code [22] was used for *ab initio* modeling of the XAFS cross section starting from these clusters. We used the IFEFFIT package (in particular Athena and Artemis) [23] to perform background subtraction and fitting, respectively. During fitting, the refined parameters were the interatomic distances and the Debye-Waller factors while coordination numbers were fixed by the crystallography and the S02 parameter was pre-evaluated by fitting the EXAFS spectrum of a Yb_2O_3 powder.

Figure 3 shows the background subtracted Yb L3-edge $k^*\chi(k)$ spectrum for the Yb:Nb:RTP crystal. For comparison, the spectra of two Yb:RTP samples with different Yb^{3+} concentrations and the spectrum of a Yb:Nb:RTP crystal grown in a solution containing WO_3 (Yb:Nb:W:RTP sample) along with the spectrum of the Yb_2O_3 standard have been included. The sample denoted as Yb:RTP(1) was grown in a solution in which a 2 mol% of TiO_2 was substituted by Yb_2O_3 , and the sample denoted as Yb:RTP(2) was grown in a solution in which 4 mol% of TiO_2 was substituted by Yb_2O_3 . Despite the sample dilution, spectra of good quality were obtained. At a first glance, one can note that the overall envelope of the signal is similar for all samples and rather close to the one of the oxide standard: such a continuously decreasing envelope is typical of an absorber atom surrounded by light neighbors and suggests that Yb binds to oxygen atoms. This is not surprising since Yb is supposed to coordinate oxygen atoms both when occupying Ti and Rb sites. However, a quantitative analysis of the spectra was necessary in order to discriminate between the two possible lattice locations.

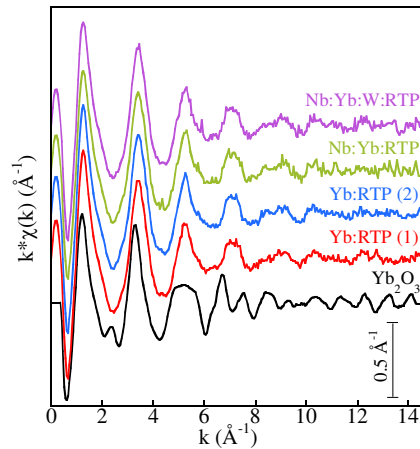


Fig. 3. Background subtracted $k^*\chi(k)$ spectra.

Figure 4 shows two fits performed on the Fourier Transform (FT) of the Yb L3-edge EXAFS spectrum for one of the samples doped with Yb only, Yb:RTP(1). The FT peaks of the experimental spectrum (continuous black line) correspond to the different atomic shells around the Yb absorber. Red circles represent a fit performed assuming that Yb was substitutional in Ti sites, while olive squares represent a model in which the dopant occupies Rb sites. EXAFS analysis could not discriminate between Yb³⁺ occupying Ti(1) or Ti(2) sites since they are locally very similar: both models reproduce very well the experimental data, just as the red circles in Fig. 4 do. However, as it is clear from the same figure, it was impossible to reproduce well the EXAFS spectrum of our sample by assuming that Yb³⁺ occupies Rb sites (olive squares). This finding was common to all the samples analyzed in this work and already gives a partial answer to the question of the dopant lattice location raised in the introduction: considering that the fits performed using the Ti substitutional model are of very good quality, this suggests that, if a part of the Yb atoms occupy Rb sites, their relative fraction must be very low and negligible with respect to that of Yb atoms occupying Ti sites. Indeed, based on EXAFS results, it is a very good approximation to affirm that Yb substitutes only Ti sites (either Ti(1) or Ti(2), or both) in all samples. This is very important for the interpretation of optical spectroscopy data, as it will be explained below.

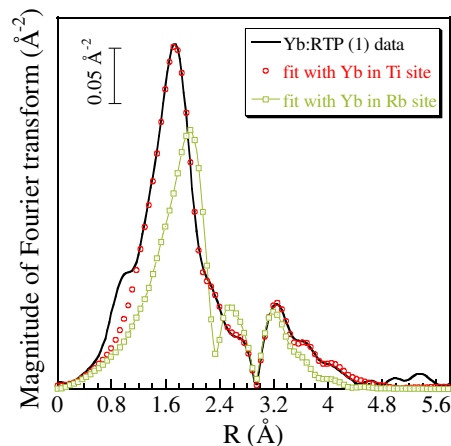


Fig. 4. Fits performed on the Fourier Transform of the EXAFS spectrum of sample Yb:RTP (1) either with a model in which Yb dopants substitute Ti atoms (red circles) or under the hypothesis of location in Rb sites (olive squares).

Figure 5 shows the fits performed for all samples with the assumption of Ti site occupation. Such fits were performed by considering EXAFS (single scattering) contribution from the first six coordination shells (O, P, Ti or Nb, O, Rb, O) for these crystals. The most important multiple scattering signals were also included in the fit. Values extracted from the fits for the structural parameters are reported in Table 1. Yb first shell was fitted by using two O sub-shells with different Yb-O bond lengths, one consisting in 1 oxygen atom at a distance $R_{\text{Yb-O}}^{1\text{st}}$ (1), the other consisting in 5 oxygen atoms at a distance $R_{\text{Yb-O}}^{1\text{st}}$ (2). By introducing more Yb-O distances the quality of the fit did not improve. We used a unique Debye-Waller factor ($\sigma_{\text{Yb-O}}^{1\text{st}}$) for the two subshells. The mean Yb-O distance for YbO₆ octahedra is larger than the Ti-O one obtained for TiO₆ octahedra in RTP [24] and Nb:RTP crystals [23], as it would be expected when introducing an additional dopant (Yb) with a larger atomic radius. We also noticed that the distribution of distances in the first Yb-O shell for these crystals is narrower compared to Ti-O distances in Yb-free samples, as it can be seen in Table 1. The maximum difference among distances in the YbO₆ octahedron is 0.159 Å, while it was 0.432 Å for RTP and 0.372 Å for Nb:RTP crystals. Then, it seems that the Yb-centered oxygen octahedra are less distorted than the Ti-centred ones, when Yb substitutes Ti in the structure. This increase of symmetry of the YbO₆ octahedra might be the explanation for the reduction of the second harmonic generation efficiency, measured in powdered samples of Yb:Nb:RTP

crystals when compared to that of RTP or Nb:RTP crystals [25], as this property has been related, traditionally, to the distortion of the TiO_6 octahedra in this family of crystals [21].

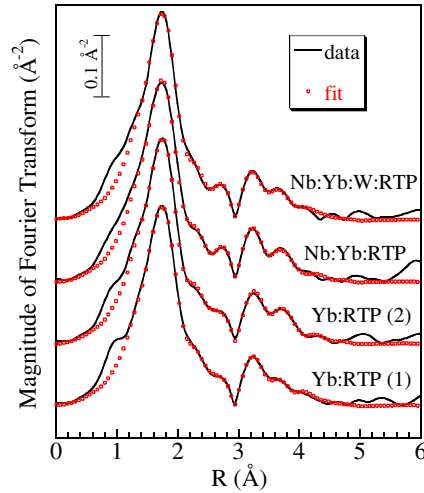


Fig. 5. Fits performed on the Fourier Transform of the EXAFS spectra of all samples assuming that Yb is substitutional to Ti. For samples containing Nb, a third shell Yb-Nb contribution to the EXAFS signal has been included in the fit.

We employed a unique second shell distance ($R_{\text{Yb-P}}^{2\text{nd}}$) and Debye-Waller factor ($\sigma_{\text{Yb-P}}^{2\text{nd}}$) while we considered two third-shell contributions in Nb-containing samples: a Yb-Ti and a Yb-Nb subshell, with the Debye-Waller factor of the latter one constrained to the one of the former, taking into account the reciprocal dependence on the reduced atomic mass [26]. The Yb-Nb Debye-Waller factor can be obtained by multiplying the Yb-Ti Debye-Waller factor of Table 1 by a factor of 0.62; such constraint has been imposed in order to minimize the number of free parameters employed in the fit. While samples doped only with Yb^{3+} were very well fitted by using the sole Yb-Ti contribution in the third shell (Fig. 4 and two bottom spectra in Fig. 5), in the Yb:Nb:RTP sample the fit quality was improved by adding a Yb-Nb contribution in the third shell in addition to the Yb-Ti one. The same behavior was observed in samples of Yb:Nb:RTP crystals grown in solutions containing WO_3 , where Yb^{3+} , Nb^{5+} and W^{6+} ions are in competition to occupy Ti positions in the structure. Figure 6 shows the fit performed on Yb:Nb:RTP and Yb:Nb:W:RTP samples with (blue circles) and without (red squares) inclusion of the Yb-Nb contribution in the third shell: it is evident that such contribution improves the agreement of the model with the experimental Fourier transform in the [2-3 Å] R -range (apparent distance), where the tail of the Yb-Nb third shell EXAFS signal resides.

Looking at Fig. 5, one can notice that, while Nb-containing samples present a well defined small peak just below 3 Å (apparent distance), Yb-single doped samples show only a shoulder in the same R -region. As suggested recently [27], this peak seems to be a signature of the Yb-Nb coordination, since it can be only reproduced by introducing a Yb-Nb third shell EXAFS signal in the fitting procedure; the spectra of Nb-free samples do not present such peak and can be very well simulated without any Yb-Nb contribution.

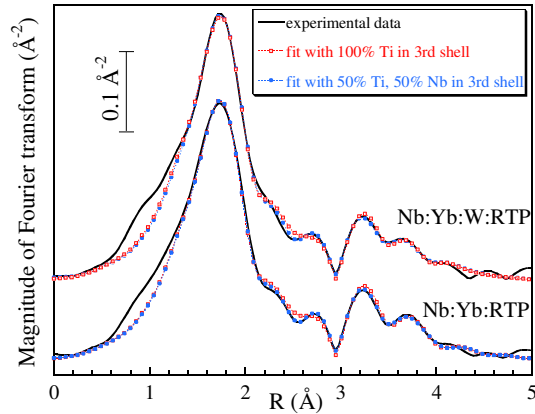


Fig. 6. Fits performed on the Fourier Transform of the EXAFS spectra of (Nb, Yb) co-doped samples assuming that Yb is substitutional to Ti. For both sample Nb:Yb:RTP and Nb:Yb:W:RTP, we show fits performed without (red squares) and with (blue circles) the third shell Yb-Nb contribution. Such contribution allows us to reproduce better the [2,3] Å R-range (apparent distance) of the experimental spectra.

In our fitting model for Nb-containing samples, the third shell was equally shared by Ti^{4+} and Nb^{5+} atoms. Considering the Nb^{5+} concentration in the samples (less than 4% with respect to Ti^{4+}), this observation gave evidence of a strong Yb-Nb ordering, with Nb^{5+} ions preferentially occupying sites close to Yb^{3+} ions. Since Nb^{5+} atoms have been always found to occupy Ti(1) positions in crystals of this family by means of X-ray and neutron diffraction [21], the Yb-Nb association suggests that Yb^{3+} in Yb:Nb:RTP crystals occupies Ti(2) sites. Furthermore, Nb^{5+} and Yb^{3+} ions seem to *attract* each other resulting in a Yb-Nb distance smaller than the Yb-Ti one. Since the atomic radii of Ti and Nb are not very different, this may be an effect related to charge compensation of the Nb^{5+} and Yb^{3+} ions. Note that, if doping and co-doping ions were randomly distributed in the crystal, with the concentrations at play, the Yb-Nb contribution would not be sufficient to give origin to the small peak below 3 Å shown in Figs. 6 and 7. As a matter of fact, a fit performed with a model which assumes random distribution of doping ions would produce a theoretical spectrum (not shown) virtually identical to the one represented by the red-squares in Fig. 7 (100% Ti atoms in the third shell).

The fits reported in this work take into account also the contribution to the EXAFS signal of oxygen atoms located at distances longer than 4 Å. Such atoms were regrouped in two subshells, the first characterized by a distance ($R_{\text{Yb-O}}^{4\text{th}}$) around 4.1 Å and the second by a distance ($R_{\text{Yb-O}}^{6\text{th}}$) at about 4.4 Å. Each of the two subshells contains 8 atoms and a unique Debye-Waller factor ($\sigma_{\text{Yb-O}}^{4\text{th}}$) was employed for the two subshells. These two O shells are separated by a Rb fifth shell; in the fit a unique variable was used to refine the Yb-Rb distance ($R_{\text{Yb-Rb}}^{5\text{th}}$) while, in order to minimize the total number of variables, the Debye-Waller factor associated to such distance ($\sigma_{\text{Yb-Rb}}^{5\text{th}}$) for all samples has been fixed to the value determined in the fit of sample Yb:RTP (1). As a matter of fact, the fit for sample Yb:RTP (1) does not involve Yb-Nb paths (and related variables), so it can accept the additional $\sigma_{\text{Yb-Rb}}^{5\text{th}}$ variable without reducing too much the degrees of freedom. Apart from the main results on the extracted structural parameters already discussed above, we also found that the Yb-Ti Debye-Waller factor is comparable to the first shell Yb-O one within the statistics uncertainty, while the Yb-P Debye-Waller factor is larger. This may give an indication of a broader distribution of P atoms in the second shell around Yb in the crystals under study. The R-factor and reduced χ^2 were comparable and sufficiently low for all fits shown in Fig. 5.

Table 1. Structural Parameters Extracted from the Fits of EXAFS Data^a

Sample	Yb:RTP(1)	Yb:RTP(2)	Nb:Yb:RTP	Nb:Yb:W:RTP
R_{Yb-O}^{1st} [Å]	2.055 ± 0.035	2.017 ± 0.020	2.044 ± 0.043	2.091 ± 0.097
R_{Yb-O}^{1st} (2) [Å]	2.184 ± 0.005	2.176 ± 0.006	2.181 ± 0.009	2.187 ± 0.009
σ_{Yb-O}^{1st} (10^{-3}) [Å ²]	3.27 ± 1.07	1.87 ± 0.60	2.64 ± 1.23	3.47 ± 2.49
R_{Yb-P}^{2nd} [Å]	3.476 ± 0.036	3.529 ± 0.036	3.461 ± 0.133	3.541 ± 0.161
σ_{Yb-P}^{2nd} (10^{-3}) [Å ²]	22.1 ± 4.7	24.0 ± 4.4	39.6 ± 11.7	38.5 ± 18.8
R_{Yb-Ti}^{3rd} [Å]	3.529 ± 0.011	3.529 ± 0.010	3.510 ± 0.053	3.555 ± 0.079
R_{Yb-Nb}^{3rd} [Å]	Not used	Not used	3.344 ± 0.024	3.329 ± 0.033
σ_{Yb-Ti}^{3rd} (10^{-3}) [Å ²]	1.96 ± 1.08	1.53 ± 0.94	2.76 ± 1.71	3.84 ± 2.64
Yb 3rd	0%	0%	50%	50%
R_{Yb-O}^{4th} [Å]	4.109 ± 0.034	4.078 ± 0.038	4.080 ± 0.061	4.121 ± 0.067
σ_{Yb-O}^{4th} (10^{-3}) [Å ²]	4.89 ± 5.62	2.41 ± 0.89	2.74 ± 1.36	4.38 ± 2.40
R_{Yb-Rb}^{5th} [Å]	4.221 ± 0.038	4.186 ± 0.056	4.183 ± 0.079	4.241 ± 0.079
σ_{Yb-Rb}^{5th} (10^{-3}) [Å ²]	8.52 ± 5.53	8.5 (fixed)	8.5 (fixed)	8.5 (fixed)
R_{Yb-O}^{6th} [Å]	4.446 ± 0.044	4.423 ± 0.043	4.418 ± 0.063	4.466 ± 0.083
RCS	4.31	6.09	3.04	6.82

Sample	R_{Yb-O}^{1st} [Å]	R_{Yb-O}^{1st} (2) [Å]	R_{Yb-O}^{1st} (3) [Å]	σ_{Yb-O}^{1st} (10^{-3})	S02
Yb ₂ O ₃	2.239 ± 0.006	2.208 ± 0.006	2.275 ± 0.006	6.49 ± 0.98	1.035 ± 0.053

^a Yb-O first shell interatomic distance [R_{Yb-O}^{1st} (1) = subshell 1, R_{Yb-O}^{1st} (2) = subshell 2], Yb-O first shell Debye-Waller factor (σ_{Yb-O}^{1st}), Yb-P second shell distance and Debye-Waller factor (R_{Yb-P}^{2nd} and σ_{Yb-P}^{2nd}), Yb-Ti third shell interatomic distance (R_{Yb-Ti}^{3rd}), Yb-Nb third shell distance (R_{Yb-Nb}^{3rd}), and Yb-Ti third shell Debye-Waller factor (σ_{Yb-Ti}^{3rd}). Oxygen atoms at distances > 4 Å are regrouped in two subshells with two Yb-O distances (R_{Yb-O}^{4th} and R_{Yb-O}^{6th}) and a single Debye-Waller factor (σ_{Yb-O}^{4th}). We report also the fifth shell Yb-Rb distance and Debye-Waller factor (R_{Yb-Rb}^{5th} and σ_{Yb-Rb}^{5th}), the percentage of Nb atoms in the third shell (Yb 3rd) used in the fit, and the reduced χ^2 (RCS) of the fit. The first shell of Yb₂O₃ is fitted using three Yb-O distances with a common increment (deltaR) and Debye-Waller factor.

4. Optical spectroscopy

The room temperature polarized absorption spectrum of the Yb:Nb:RTP crystal was measured with a Varian Cary 500 spectrophotometer. The polarization of the incident beam was controlled with a Glan-Taylor polarizer. The sample was cut as a cube crystallographically oriented, with dimensions of 3 mm × 2.5 mm × 3 mm along the $a \times b \times c$ crystallographic directions. The measurements were made by polarizing the electric field of the incident beam parallel to the b crystallographic direction ($E//b$) with propagation of light along the a direction. Since Yb³⁺ does not present different optical absorption peaks along different polarizations, and the only difference among the different polarization configurations would be the intensity of the different peaks, the characterization of one of their polarizations was sufficient to provide the position of the different peaks of the optical absorption spectrum, important for our analysis.

The unpolarized fluorescence spectrum of Yb³⁺ in Yb:Nb:RTP crystals was recorded at room temperature between 950 and 1100 nm in a 90° geometry with excitation at 902.2 nm with a Ti:sapphire laser modulated at 1 kHz. The fluorescence was dispersed by a double monochromator (Jobin Yvon-Spex HR460), with a focal length of 0.46 m, and detected by a cooled Hamamatsu NIR R5509-72 photomultiplier which was connected to a lock-in amplifier.

In the lanthanides series, Yb³⁺ is distinguished the strong dependence of its spectroscopy on the host matrix. It is of special interest to study the broadening of the absorption and emission bands due to Stark splitting of the degenerate levels of its fundamental and excited states, ²F_{7/2} and ²F_{5/2}, respectively, which is related to the crystal field strength induced by the ions of the matrix and also, the existence or not, of disorder or multiple positions for the rare earth site.

Yb³⁺ ions in Nb:RTP substitute Ti⁴⁺ ions in the structure, as EXAFS results have demonstrated (Ionic radii $r_{Yb^{3+}} = 0.861\text{Å}$, coordination number c.n. = 6; $r_{Ti^{4+}} = 0.605\text{Å}$, c.n. =

6). As explained above, in the structure of Nb:RTP, as well as in the other crystals of the KTP family, two Ti non equivalent sites exist, which are labeled as Ti(1) and Ti(2) [21]. These two sites have C_1 local site symmetry, and hence the maximum number of bands for the ${}^2F_{5/2}$ excited state of Yb^{3+} would be $(2J + 1)/2$, i.e. three bands for each spectroscopic site. If Yb^{3+} occupies the two Ti positions in the crystalline structure, six bands should be expected to appear in the absorption spectrum. However, if it occupies only one Ti position in the structure, only three bands would be expected to appear in the absorption spectrum. Furthermore, since the Ti(2)O₆ octahedron is less distorted than the Ti(1)O₆ one, with an average Ti-O distance longer than that of the Ti(1)O₆ octahedron, a weaker crystal field would be expected to influence Yb^{3+} if the Ti(2) position is occupied. EXAFS results have shown the following: if Nb⁵⁺ is going to Ti(1) positions, as it has been demonstrated for Nb:RTP and Er:Nb:RTP crystals [21,28], then the Yb^{3+} necessarily has to go to Ti(2) positions, occupying the less distorted and weaker crystal field position. This behavior is due to the short range ordering between Nb⁵⁺ and Yb^{3+} in this structure. So, only three bands would be expected in the absorption spectra of this ion in these crystals.

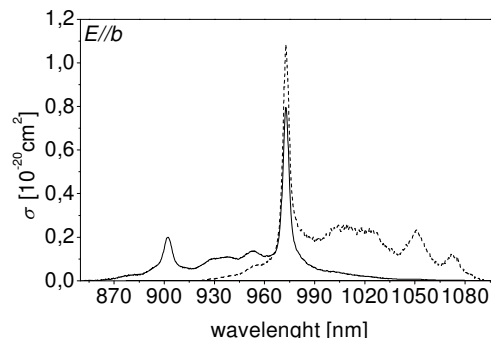


Fig. 7. Absorption (solid line) and emission (dashed line) cross-sections at room temperature of a Yb:Nb:RTP crystal.

Figure 7 shows the absorption and emission cross section spectra (${}^2F_{7/2} \leftrightarrow {}^2F_{5/2}$) of Yb^{3+} in Yb:Nb:RTP measured at room temperature with $E//b//y$ dielectric axis and recorded in the wavelength range 850-1100 nm. Since ytterbium has an odd number of electrons in the 4f shell, polarization-dependent selection rules for the electronic transitions are not expected, and the number and positions of the absorption and emission peaks have to be independent of the polarization, although their intensity can still vary. So, by studying one of the three possible polarizations, is sufficient to gather the information that is needed. As mentioned before, the number of Kramers doublets expected for only one Yb^{3+} site (local site symmetry C_1) is three and correspond to the three main peaks of the absorption spectra we observed. However, in the absorption spectrum of Yb^{3+} in Yb:RTP crystals [27], six peaks have been observed instead. Three of them were equivalent to those observed in the absorption spectrum measured in Yb:Nb:RTP crystals. This implies in fact that, as we expected from the results obtained by EXAFS, Yb^{3+} is located only in one of the two Ti positions available in the structure of the Yb:Nb:RTP crystals. Furthermore, the splitting of the three levels observed in this crystal is smaller than the splitting of the additional three levels observed in the Yb:RTP crystal. This would be a consequence of the weaker crystal field that Yb^{3+} experiences in the location it occupies in the Yb:Nb:RTP crystals, indicating that Yb^{3+} is located in the Ti(2) position, that is being in the less distorted position, as we explained before. This is in agreement with the results we obtained by EXAFS.

The maximum absorption and emission cross section for $E//b$ at room temperature equal 0.795 and $1.084 \times 10^{-20} \text{ cm}^2$, respectively, centered at 972.8 nm corresponding to the zero phonon line. The emission cross section was calculated using the Füchtbauer-Ladenburg

method. The room temperature zero phonon linewidth (FWHM) of this peak in Yb:Nb:RTP crystals was measured to be 4.2 nm.

This crystal presents very broad and smooth emission spectra, extending from around 930 nm to more than 1080 nm. According to the results obtained in this paper, this broad emission spectrum is due to the electronic structure of Yb³⁺ in these crystals, and more specifically to the large splitting (956 cm⁻¹) of the ytterbium ground state (²F_{7/2}). It is not related to a multisite effect, i.e. Yb³⁺ being located in multiple spectroscopic sites. This large splitting plays a significant role to reduce the thermal population in the lower laser state in this quasi-three-level nonlinear host laser material. This large splitting is similar to that observed in Yb-doped fluoroapatites [29], Yb-doped Ca₈La₂(PO₄)₆O₂ oxyapatite [30] or Yb-doped sesquioxides [31] and indicates that the broadband fluorescence observed is interesting for tunability and subpicosecond-pulse generation applications.

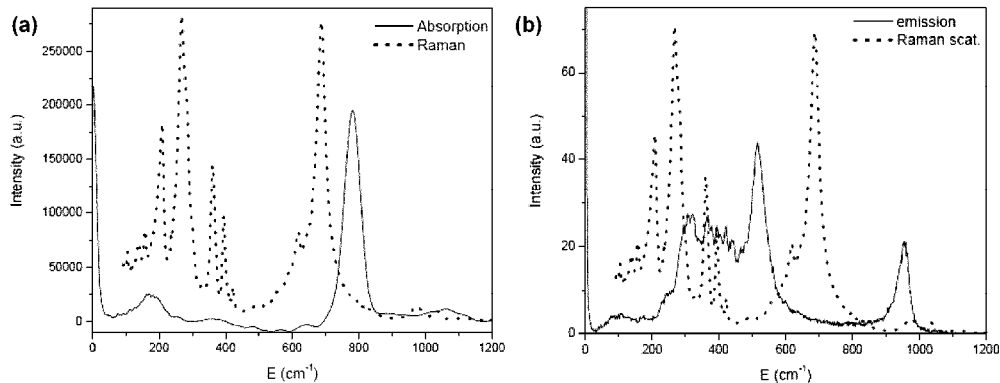


Fig. 8. Comparison of (a) the absorption, and (b) the emission of Yb³⁺ in Yb:Nb:RTP crystals at 6 K including the Raman scattering of the crystal (dotted line).

Furthermore, we explored a possible thermal broadening of the peaks at temperatures between 6 and 300 K. No significant effects were observed for absorption spectra, while some broadening is apparent in the region between 970 and 1000 nm of the emission spectra [13], resulting in a smooth spectrum. For this reason we checked for the phonon-electron-coupled transitions, which are important in the Ln³⁺ ions located at the beginning and the end of the lanthanide series [32] and can affect the splitting of the electronic levels of Yb³⁺. These effects can give rise to strong vibronic sidebands or to the deformation or splitting of electronic lines in the resonant coupling which could complicate the spectra. For this purpose we compared the absorption and emission spectra of Yb³⁺ in Yb:Nb:RTP crystals recorded at low temperature with the Raman scattering of this crystal (see Fig. 8) by adjusting them to the same energy scales, and taking the origin at the 0-line energy. Since it is not evident the existence of a shift of the zero line transition at 6 K, these results would indicate that if we do not take into account the self-trapping effect, there would not be resonant interactions implied between the (0) → (0') transitions of the ²F_{5/2} and ²F_{7/2} manifold of Yb³⁺ in these crystals. However, by comparing the luminescence spectrum at low temperature and the Raman scattering, we can attribute some of the low intensity lines observed in the spectrum, and located below 400 cm⁻¹, to electron-phonon coupling between the active ions and the matrix. When the difference between two Stark levels matches the energy of a lattice phonon, a strong vibronic structure can appear in the spectra. This leads to a splitting of the bands and in some cases even makes it difficult to determine the energy level. As the electron-phonon coupling we observed only affects the least intense peaks and we did not take into account self-trapping effects, we think that re-absorption effects related to new transitions from thermally populated ground state sublevels should be weak in these crystals, although they can contribute to the

broadening and smoothening of the spectra in the region between 970 and 1000 nm observed previously [13].

So, after all this spectroscopic characterization, we can propose the energy diagram for Yb^{3+} in Yb:Nb:RTP crystals shown in Fig. 9, that describes the large splitting for the different energy levels observed for this ion in these crystals. Due to the crystal field, the ${}^2F_{7/2}$ ground level of Yb^{3+} splits in 4 energy levels at energies of 309, 521 and 956 cm^{-1} , taking as the origin of energies the position of the ${}^2F_{7/2}$ (0) level. The ${}^2F_{5/2}$ excited state is apart by 10289 cm^{-1} from the ground state, and splits in 3 energy levels lying at 10289 cm^{-1} (${}^2F_{5/2}$ (0')), 10471 cm^{-1} (${}^2F_{5/2}$ (1')), and 11069 cm^{-1} (${}^2F_{5/2}$ (2')), respectively.

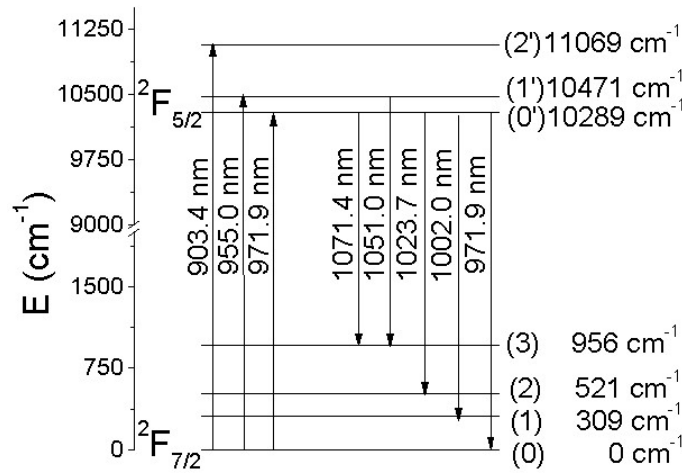


Fig. 9. Energy diagram of Yb^{3+} in Yb:Nb:RTP crystals.

5. Mode-locked laser operation

Mode-locked laser operation of the Yb:Nb:RTP crystal was studied by placing it in an astigmatically compensated z-shaped optical cavity.

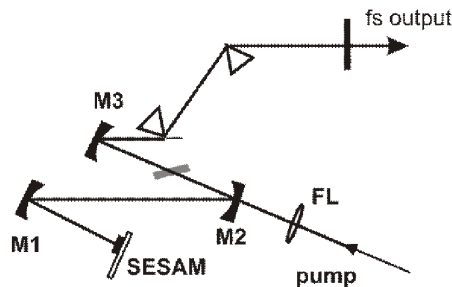


Fig. 10. Laser setup used for the Yb:Nb:RTP laser.

The pump source was a home-made Ti:sapphire laser with a maximum power (incident on the crystal) of 1.9 W at the optimum pump wavelength of 972.7 nm. The absorption cross-section at this wavelength amounted $0.795 \times 10^{20} \text{ cm}^2$. The pump beam was focused onto the crystal using a 6.28 cm focusing lens. The 3 mm thick, uncoated, a -cut crystal with an Yb density of $1.9 \times 10^{20} \text{ at}\cdot\text{cm}^{-3}$ was placed at Brewster angle so that both the pump (972.7 nm) and laser radiation (1053 nm) were polarized parallel to the crystal b -axis, since this is the

configuration that allowed to reach the maximum absorption. No special cooling was applied. The two folding mirrors had a radius of curvature (RC) of 100 mm, and whereas M2 was antireflection coated for the pump wavelength while highly reflecting at the laser wavelength. A third mirror with a RC = -150 mm was used to create a focus on the semiconductor saturable absorber mirror (SESAM) which terminated the cavity (Fig. 10). A plane output coupler with transmission of 0.4% was used in the other cavity arm which contained two SF10 Brewster prisms, separated by 46 cm, for dispersion compensation.

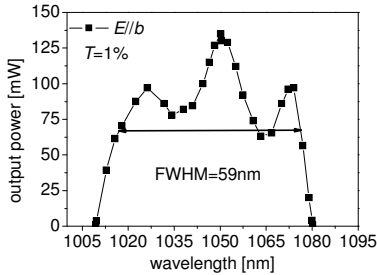


Fig. 11. Tuning range of the continuous-wave Yb:Nb:RTP laser obtained with a two-plate Lyot filter.

The efforts done to dope Nb:RTP with ytterbium ions had led recently to the demonstration of its continuous-wave (CW) laser operation with a maximum output power of 154 mW, a maximum slope efficiency of 60.1% and a laser threshold as low as 18 mW [18]. The obtained results depend on the output coupler used and the orientation of the crystal. The highest output power was obtained for polarization $E//b$ and an output coupler of 1%. The tuning range in that case (see Fig. 11), extends from 1009 to 1080 nm with a FWHM of 59 nm. This clearly indicates the suitability of this novel Yb-doped crystal for the generation of femtosecond laser pulses. This broad tunability is due to the large splitting (956 cm^{-1}) of the ytterbium ground state ($^2F_{7/2}$), as demonstrated in the previous section.

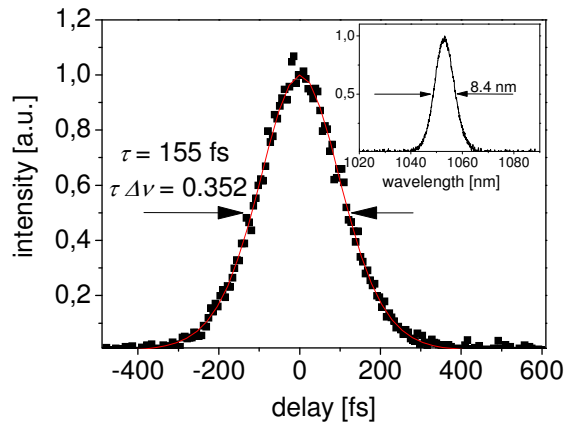


Fig. 12. Autocorrelation trace (symbols) with a fit (line) of the shortest pulses and the corresponding laser spectrum (inset) (τ – pulse duration, $\tau\Delta\nu$ – time-bandwidth product).

By adding a SESAM and two dispersion compensating prisms to the optical cavity (see Fig. 10), the Yb:Nb:RTP sample started to operate in the mode-locked regime, delivering pulses with a duration (FWHM) of 155 fs, assuming sech^2 pulse shape (Fig. 12), which were very stable in time, without any trend of Q-switching, notwithstanding the relatively long fluorescence lifetime of 2.2 ms [33]. However, the average output power at the repetition rate of 96 MHz was only 5 mW. This was due to the low output coupler transmission which had to be used in order to compensate for the additional cavity losses having in mind the low crystal

absorption and gain. The pulse spectrum was centered at 1053 nm and was 8.4 nm broad (FWHM), so that the time-bandwidth product amounts to 0.352, which means slightly above the value of 0.315 for Fourier limited pulses, indicating that further compression could be possible.

While in CW regime only weak green up-converted fluorescence was visible in the crystal, when mode-locking occurred, bright green light from the crystal was observed. This non phase-matched second-harmonic generation greatly facilitated the alignment of the laser for shortest pulses.

6. Conclusions

In conclusion we have generated 155 fs long laser pulses at 1053 nm with the acentric Yb:Nb:RTP crystal, mode-locked with a SESAM. Further work will be devoted to increase the output power by increasing the laser gain (by increasing either the doping level or the crystal thickness) and pumping with a laser diode. However, the increasing of the doping level seems not to be an easy task, and we are exploring different strategies such as the replacement of Nb⁵⁺ by Ta⁵⁺ in the crystals [34]. Of the very few non-centrosymmetric crystals demonstrated to be lasing with the Yb-dopant, Nb:RTP is the 4th one besides the borates YAl₃(BO₃)₄ (YAB), Ca₄GdO(BO₃)₃ (GdCOB) and Ca₄YO(BO₃)₃ (YCOB), with which mode-locked operation has been achieved.

The pathway leading to the creation of this laser has passed through several characterization steps (micro-structural, electrical, and optical) that allowed us to understand the physical origin of the broad emission band of Yb³⁺, which is the basis for the generation of femtosecond laser pulses. At least for the dopant concentration range we have examined, broad emission is due to the large splitting of ytterbium ground state and not to the presence of ytterbium ions in different crystallographic sites. Some resonant phonon-electron coupled transitions were observed for Yb³⁺ in these crystals that can also contribute to the broadening of the emission spectrum.

Acknowledgments

We acknowledge the European Synchrotron Radiation Facility (ESRF) for provision of beamtime at the BM29 beamline via project HS-3076. This work was supported by the Spanish Government under projects MAT2008-06729-C02-02/NAN and the Catalan Authority under project 2009SGR235. J. J. Carvajal and M. C. Pujol are supported by the Education and Science Ministry of Spain and European Social Fund under the Ramon y Cajal program, RYC2006 – 858 and RYC2004 – 1453, respectively.